J. Phys. B: At. Mol. Opt. Phys. **31** (1998) 3997–4016. Printed in the UK PII: S0953-4075(98)93467-8

Coherent fan emissions

A I Lvovsky and S R Hartmann
Department of Physics, Columbia University, New York, NY 10027, USA

Received 21 April 1998

Abstract. A transient grating is induced at $t = 0$ in an optically thin caesium vapour sample using two simultaneous intense short laser pulses which are resonant with the fundamental $6S_{1/2}$–$6P_{1/2}$ transition and characterized by the wavevectors $\vec{k}_1$ and $\vec{k}_2$. These pulses are followed by a third resonant excitation pulse at $t = \tau$ with wavevector $\vec{k}_3$. Prompt and delayed super-radiant emissions follow with a spatial pattern governed by higher-order diffraction effects. We study the polarization and modulation properties of these coherent fan emissions.

1. Introduction

The transient induced grating technique has been widely used for exploration of ultrafast relaxation phenomena in various media [1–3]. Two simultaneous noncollinear pulses entering a sample induce coherence in the form of a transient grating. A third pulse probing the sample is diffracted by the grating and scattered by $\vec{k}_2 - \vec{k}_1$. The intensity of the diffracted field measured as a function of the third pulse's delay yields the coherence relaxation rate.

This technique can be considered as a special case of the three-pulse stimulated photon echo method. Here the first excitation pulse produces a coherent superposition between the ground and excited states which is then transferred by the second excitation pulse into a coherent superposition separately between the ground states and between the excited states. In this manner excited and ground state gratings have been formed. The relaxation rate of either the ground state or excited state coherent superposition is generally much slower than that of a ground–excited state superposition. Therefore to study grating relaxation it is necessary that the second excitation pulse immediately follows the first. This is the motivation for applying the first two pulses simultaneously.

When the temporally overlapping excitation pulses are intense the gratings produced scatter in many orders and echo experiments become very rich [4, 5]. In [4] standing wave excitation pulses were generated by deploying temporally overlapping laser pulses into the sample from opposing directions. A multitude of echoes were produced at times $t_e = \tau(1 + n_1/2n_2)$, where n_1 and n_2 are arbitrary integers, when two such pulses separated by τ were used.

In this paper we excite a caesium vapour sample with nearly collinear pulses and examine the temporal characteristics of the many super-radiant emissions which occur in the various diffraction orders. At $t = 0$ we apply a simultaneous pulse pair with wavevectors $\vec{k}_1$ and $\vec{k}_2$ followed at $t = \tau$ by a third with $\vec{k}_3$. Prompt emissions appear at $t = 0$ and τ and a delayed emission appears at 2τ. For the excitation pulses we use, these emissions appear in a fan-like array and are called coherent fan emissions (CFE). The CFE at $t = 0$ are called fan free decays (FFD) while those at τ and 2τ are called fan photon echoes (FPE).

0953-4075/98/173997+20$19.50

2. Theory

The foregoing theoretical analysis consists of two parts. In the first part, we get some insight into the physics of CFE by considering their formation on a simple two-level system. In the second, we develop the technique for exact quantitative analysis of CFE in caesium vapour.

2.1. The origin of the fans

2.1.1. Billiard-ball echo model. Our theoretical analysis uses the billiard-ball model [6–8] of coherent phenomena in gases since it provides a simple means of presenting an otherwise complicated experiment. The idea is to represent each atom in the sample by a wavepacket (whose size is determined by the thermal distribution of atomic momenta) and to follow its development in time as it is subjected to short (compared with the inverse Doppler width) optical excitation pulses. Each excitation pulse will generate additional wavepackets which represent the new states the initial wavepacket has been coupled to by the pulse. All wavepackets recoil according to the momentum of the photon absorbed or emitted. When a sequence of excitation pulses is applied, the initial wavepacket divides and redivides with the result that the several wavepackets that have been produced separate, recombine, separate again and so on. Associated with overlapping wavepackets is a macroscopic dipole moment which can generate super-radiant emission. Thus by simply following the wavepacket (billiard-ball) trajectories and noting when they cross one discovers the temporal development of these emissions. These trajectories are displayed in a recoil diagram which also serves as a Feynman diagram [7]. This recoil diagram shows the billiard-ball-centre displacements as a function of time.

The degree of wavepacket overlap is determined by associating, with each trajectory, a billiard ball whose density as a function of $\vec{r}$ is given by

$$\rho(\vec{r}-\vec{r}_j)=\left(\sqrt{\frac{\pi}{2}}R_{\mathrm{BB}}\right)^{-3/2}\mathrm{e}^{-(\vec{r}-\vec{r}_j)^2/R_{\mathrm{BB}}^2}, \tag{1}$$

where $R_{\mathrm{BB}}=\hbar/\sqrt{m_{\mathrm{Cs}}k_{\mathrm{B}}T}$ is the billiard-ball radius, m_{Cs} is the mass of an atom (caesium in our case), k_{B} is the Boltzmann constant, T is the temperature and $\vec{r}_j$ lies on the trajectory. When billiard balls of trajectories i and j overlap a macroscopic dipole moment is formed whose amplitude is proportional to the integral

$$f_{ij}=\int\rho(\vec{r}-\vec{r}_i)\rho(\vec{r}-\vec{r}_j)\,\mathrm{d}^3\vec{r}=\mathrm{e}^{-(\vec{r}_i-\vec{r}_j)^2/(2R_{\mathrm{BB}}^2)}. \tag{2}$$

All that is necessary for sizable super-radiance to occur is that the trajectories come within R_{BB} of each other (exact crossing is not required).

In an optically thin gas (such as in our experiment), Doppler dephasing determines the duration of super-radiant emissions. One way of estimating the Doppler dephasing time is to divide the optical wavelength by the thermal velocity. Another (as in the billiard-ball method) is to divide the de Broglie wavelength of the atomic wavepacket (R_{BB}) by the atomic recoil velocity. Both methods give identical results.

An example is shown in figure 1 which displays a complete recoil diagram for a conventional stimulated photon echo experiment in which excitation pulses are applied at $t=0$, τ_1 and τ_2. Whenever a laser pulse hits the sample, each trajectory in the diagram splits into two branches that correspond to the excited and ground state billiard balls. The intersection of any two trajectories indicates that the associated billiard balls have come into overlap so that there may be a burst of coherent radiation from the sample.

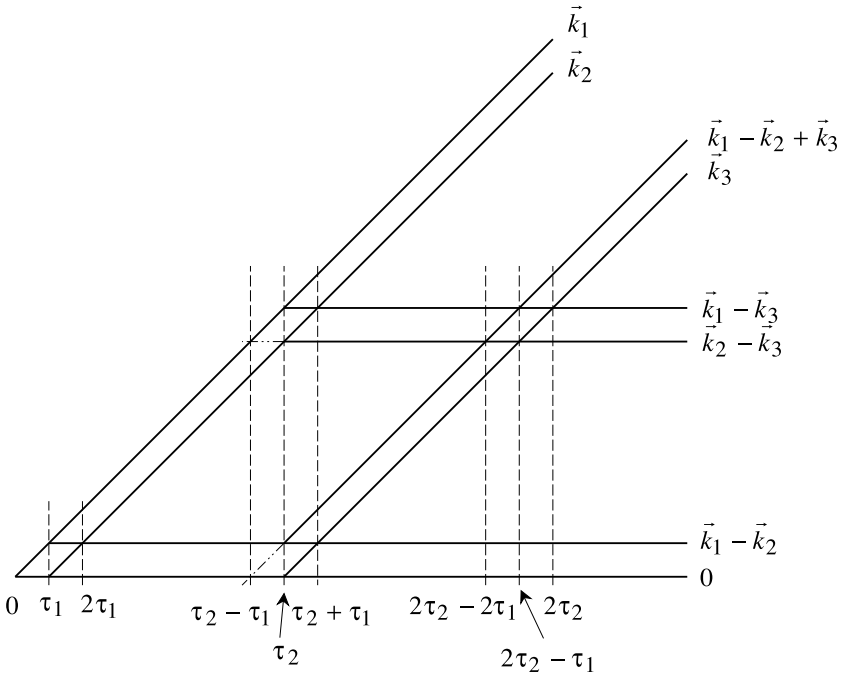

Figure 1. A recoil diagram for a conventional stimulated photon echo experiment with excitation pulses applied at $t = 0$, τ_1, and τ_2. The simulated echo appears at $t = \tau_1 + \tau_2$ and the normal two-pulse echo at $t = 2\tau_1$. In addition to these conventional echoes this diagram shows that echoes are to be expected at $t = 2\tau_2 - 2\tau_1$, $2\tau_2 - \tau_1$, and $2\tau_2$. If $\tau_1 \leqslant T_2^*$ there is also a prompt coherent scattering at $t = \tau_2$ from the grating produced by the initial pulse pair. This scattering can be associated with extrapolated crossings at $t = \tau_2 - \tau_1$.

2.1.2. Stimulated echo pulse sequence. Referring to figure 1, we first assume that the separation τ_1 between the first two pulses is much smaller than the delay τ_2 of the third pulse and both τ_1 and τ_2 are substantially greater than the inhomogeneous dephasing time T_2^*:

$$T_2^* \ll \tau_1 \ll \tau_2. \tag{3}$$

In other words, we assume that the two billiard balls created by the first pulse have enough time to drift apart before the sample is hit by the second one.

In this case, there is a photon echo associated with each crossing (the noncollinearity of the excitation pulses is so slight that it can be neglected) of the figure 1 recoil diagram trajectories. The wavevector associated with each echo is equal to the difference between the wavevectors of the crossing trajectories. The crossing at $t = 2\tau_1$, for example, corresponds to the two-pulse echo phased to radiate at $2\vec{k}_2 - \vec{k}_1$, two crossings at the moment $t = \tau_1 + \tau_2$ are associated with the stimulated photon echoes, and a series of crossings near $t = 2\tau_2$ result in two-pulse echoes caused by one of the first two and the third excitation pulses.

The situation changes if inequality (3) is modified in the following manner:

$$\tau_1 \lesssim T_2^* \ll \tau_2, \tag{4}$$

so that the two billiard balls created by the first excitation pulse still overlap when the second pulse arrives. In figure 1 the trajectories associated with wavevectors 0 and $\vec{k}_1 - \vec{k}_2 + \vec{k}_3$ technically do not cross. However, at the moment $t = \tau_2$ the two billiard balls represented

by these trajectories still do overlap resulting in the prompt scattering of the third pulse along $\vec{k}_3 + (\vec{k}_1 - \vec{k}_2)$. This signal can be associated with the extrapolated crossing at $t = \tau_2 - \tau_1$.

2.1.3. Induced grating limit. The situation becomes even more interesting when $\tau_1 = 0$, i.e. the first two pulses overlap. The sample is now simultaneously exposed to photons with wavevectors $\vec{k}_1$ and $\vec{k}_2$. An atom absorbing n of the former and emitting m of the latter will recoil with momentum $\hbar(n\vec{k}_1 - m\vec{k}_2)$. The case where the former are emitted and the latter are absorbed is obtained by making n and m negative. For $|n - m| = 0$ the atom remains in the ground state, for $|n - m| = 1$ it is excited. The various trajectories corresponding to different values of n and m form a fan (see figure 2). Here we have labelled the recoiling trajectories with the k vectors $(n + 1)\vec{k}_1 - n\vec{k}_2$ and the ground state trajectories with the k vectors $n\vec{k}_1 - n\vec{k}_2$, n being an integer associated with each trajectory. Since the trajectories are four dimensional we display them by showing their three projections in figures 2(*b*)–(*d*). Note that in these figures we have exaggerated the differences in the wavevectors so that the diagrams are easier to read. Actually, the difference is so small that if the trajectories had been drawn to scale they would not appear to fan out.

2.1.4. Free decay. Billiard balls associated with the various trajectories overlap at $t = 0$ and then separate as the trajectories diverge. The overlap of billiard balls associated with adjacent ground and excited state trajectories leads to a fan of coherent emissions along $(n_1 + 1)\vec{k}_1 - n_1\vec{k}_2 - n_2(\vec{k}_1 - \vec{k}_2) = (\Delta n + 1)\vec{k}_1 - \Delta n\vec{k}_2$ where $\Delta n = n_1 - n_2$ is a positive or negative integer. These FFDs are the optical analogues of the free induction decays of nuclear magnetic resonance.

The difficulty with the experimental observation of a free decay (FD) is that it is easily masked by the excitation pulse which induces it. Typically, the intensity of the excitation pulse is at least an order of magnitude greater than that of the FD. For an excitation pulse short enough to cover the optical resonance lineshape, the FD will last for T_2^*, but T_2^* is usually too short to enable one to disentangle the FD from the excitation pulse and consequently masking occurs.

The first FD observation [9] succeeded by only exciting a small fraction of the resonance lineshape so that the FD persisted long after T_2^*. More recently the FD associated with a second harmonic signal was made possible without recourse to a partial excitation of the resonance lineshape by exploiting the difference in the frequencies of the excitation pulse and FD signals [10].

The transient induced grating technique, which we have discussed here, offers another way of observing a FD. Since the FFDs are simply an array of FDs, directed along $\vec{k}_1$, $\vec{k}_2$, $2\vec{k}_2 - \vec{k}_1$, $3\vec{k}_2 - 2\vec{k}_1$ etc, all except those directed along $\vec{k}_1$ and $\vec{k}_2$ can be spatially separated from the intense excitation pulses.

2.1.5. Stimulated echo fan. After applying an excitation pulse at $t = 0$ with two noncollinear components along $\vec{k}_1$ and $\vec{k}_2$ a third pulse is applied at $t = \tau$ along $\vec{k}_3$. As shown in figure 2, each of the original fans then branches to produce new fans along $(n+1)\vec{k}_1 - n\vec{k}_2 - \vec{k}_3$ and $n(\vec{k}_1 - \vec{k}_2) + \vec{k}_3$ according to whether the photon stimulates emission or is absorbed. Prompt coherent emissions are again produced by the overlap of billiard balls associated with adjacent trajectories, keeping in mind that the angular spread of any fan is so small that it does not lead to any additional reduction in billiard-ball overlap. The upper branch leads to emissions along $(n_1+1)\vec{k}_1 - n_1\vec{k}_2 - ((n_2+1)\vec{k}_1 - n_2\vec{k}_2 - \vec{k}_3) = \vec{k}_3 + \Delta n(\vec{k}_1 - \vec{k}_2)$

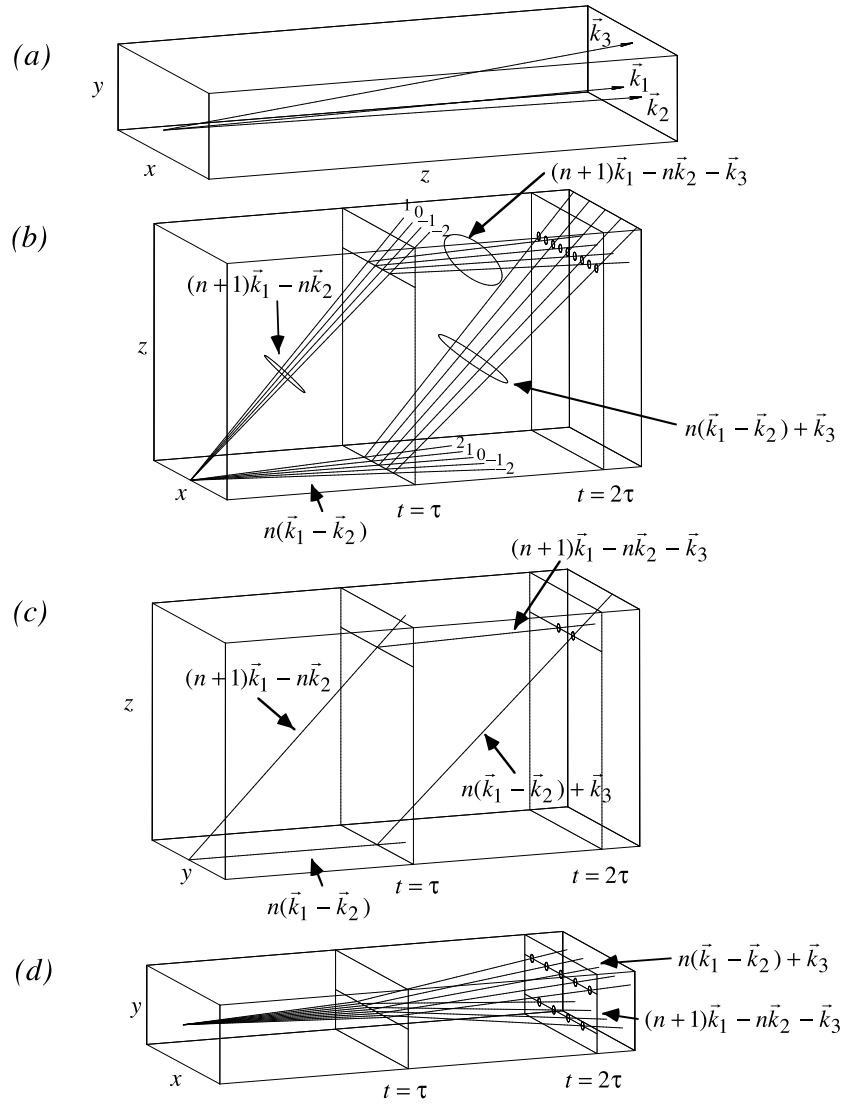

Figure 2. Three projections of a four-dimensional recoil diagram associated with excitation pulses applied along $\vec{k}_1$, $\vec{k}_2$ and $\vec{k}_3$ at times $t = 0$, 0 and τ. Each trajectory is labelled with an integer n and the k vector of each trajectory is given as a function of n. The angular separation of the wavevectors is greatly exaggerated to enable the different trajectories to be distinguished. (*a*) The orientation of the k vectors is displayed. (*b*) The z, x recoil displacement is given as a function of t. (*c*) The z, y recoil displacement is given as a function of t. (*d*) The y, x recoil displacement is given as a function of t.

as does the lower branch since $n_2(\vec{k}_1 - \vec{k}_2) + \vec{k}_3 - n_1(\vec{k}_1 - \vec{k}_2) = \vec{k}_3 + \Delta n(\vec{k}_1 - \vec{k}_2)$. These are prompt scatterings of the third pulse off the grating produced by the first complex pulse and are related to the stimulated echo in the manner described previously.

2.1.6. Two-pulse photon echo fan. In the neighbourhood of $t = 2\tau$ the fan trajectories created by the pulse at $t = \tau$ effectively cross to produce an echo emission array along

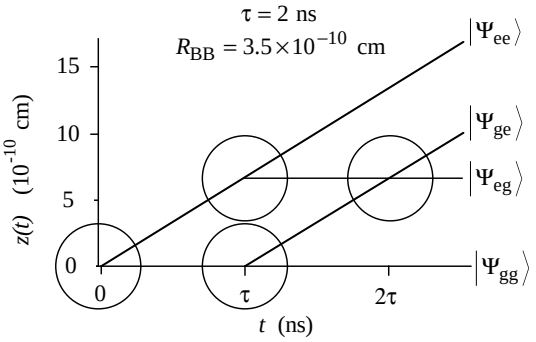

Figure 3. A correctly scaled recoil diagram specialized to the Cs vapour $6S_{1/2}$–$6P_{1/2}$ transition at 320 K for $\tau = 2$ ns. The 'fan' of propagators associated with the transient induced grating is unresolved. The four circles at the trajectory crossing points represent the billiard balls, also drawn to scale. R_{BB} denotes the billiard-ball radius.

$n_1(\vec{k}_1 - \vec{k}_2) + \vec{k}_3 - ((n_2 + 1)\vec{k}_1 - n_2\vec{k}_2 - \vec{k}_3) = 2\vec{k}_3 + (\Delta n - 1)\vec{k}_1 - \Delta n\vec{k}_2$. These are the analogues of the normal two-pulse photon echo.

2.1.7. Fan divergence exaggeration. As previously noted, figure 2 greatly exaggerates the separation between recoil trajectories corresponding to different fan components within the same quantum state. In our experiment, the angle between $\vec{k}_1$ and $\vec{k}_2$ is about 0.003 rad which is equal to the angular separation between the recoil trajectories. Drawn to this scale the fans in figure 2 would coalesce to a single trajectory. It suffices then to draw a two-dimensional recoil diagram which we do in figure 3, specializing to $\tau = 2$ ns. The ordinate representing the recoil displacement corresponds to the direction of the laser pulses. In this figure, which has been drawn to scale, we show the outline of the billiard ball (1) representing atoms in a Cs atomic vapour at 45 °C.

It follows that in calculating coherent emission intensity the displacement of billiard balls associated with angling between $\vec{k}_1$, $\vec{k}_2$ and $\vec{k}_3$ can be neglected, so that the recoil velocity is $\vec{v}_{recoil} \approx \hbar\vec{k}/m_{Cs}$ for the excited state billiard balls and zero for the ground state ones. The billiard balls associated with different trajectories of the same branch can be considered completely overlapping.

2.2. The calculation of fans

2.2.1. Fundamental transition in caesium. We work on the $6S_{1/2}$–$6P_{1/2}$ transition in caesium vapour. As shown by the photon echo experiments [11] on the same transition, this system is very well understood and therefore a well-suited medium for conceptual experiments involving physics of coherent phenomena. Both ground and excited levels of the transition contain two magnetic substates with quantum number m_J equal to $\frac{1}{2}$ and $-\frac{1}{2}$; in addition, each level is split into two sublevels due to hyperfine interaction.

Since the nuclear spin of Cs is $I = \frac{7}{2}$, the quantum numbers F of the hyperfine sublevels are 3 and 4 for both 6S and 6P states. The magnitude of hyperfine splitting is 9.193 GHz for 6S and 1.168 GHz for 6P [12] and for both levels, the $F = 4$ sublevel lies above the $F = 3$. Our excitation pulses are very short in comparison with the periods of the above frequencies. One can therefore neglect the hyperfine interaction while the excitation pulse is applied and assume that all hyperfine levels are equally excited. On the other hand, since the splitting frequencies substantially exceed the inverse delay between excitation pulses, the quantum number m_J is not conserved after an excitation pulse and super-radiant emissions exhibit dramatic modulation effects [11].

2.2.2. Optical excitation by two simultaneous pulses. Consider a caesium sample being resonantly excited at $t = 0$ by two laser pulses with equal electric field amplitude $E_{(12)}$ and slightly noncollinear wavevectors $\vec{k}_1$ and $\vec{k}_2$. We choose our reference frame so that the z-axis coincides with the pulses' propagation direction (neglecting their small angular separation) and the x-axis is along the electric field polarization of the third excitation pulse, as well as the direction of $\vec{k}_2 - \vec{k}_1$. We assume that the first and second laser pulses are both linearly polarized at angles α_1 and α_2, respectively, to the x-axis. In the plane wave approximation the electric field at some point $\vec{r}$ in the sample is given by

$$\vec{E} = E_{(12)}(\hat{x}\cos\alpha_1 + \hat{y}\sin\alpha_1)\mathrm{e}^{\mathrm{i}(\vec{k}_1\cdot\vec{r}-\omega t)} + E_{(12)}(\hat{x}\cos\alpha_2 + \hat{y}\sin\alpha_2)\mathrm{e}^{\mathrm{i}(\vec{k}_2\cdot\vec{r}-\omega t)}, \tag{5}$$

where $\hat{x}$ and $\hat{y}$ are unit vectors along the x- and y-axes, respectively. We expand (5) into a sum of two orthogonal circularly polarized electromagnetic plane waves whose components are written as

$$\vec{E} = \vec{E}_+ + \vec{E}_-, \tag{6}$$

with

$$E_\pm = \frac{E_{(12)}}{2}(\hat{x} \pm \mathrm{i}\hat{y})(\mathrm{e}^{\mathrm{i}(\vec{k}_1\cdot\vec{r}-\omega t\mp\alpha_1)} + \mathrm{e}^{\mathrm{i}(\vec{k}_2\cdot\vec{r}-\omega t\mp\alpha_2)}), \tag{7}$$

where subscripts '+' and '−' stand for the counterclockwise and clockwise circular polarizations, respectively, as viewed from the positive z-direction. Since the quantization axis z is chosen along the pulse propagation direction, the counterclockwise polarized component of the electromagnetic field contains only photons with the z-component of the spin equal to $+1$, and therefore excites only the transition $|6\mathrm{S}, m_J = -\frac{1}{2}\rangle \rightarrow |6\mathrm{P}, m_J = +\frac{1}{2}\rangle$. Similarly, the clockwise field affects only the $|6\mathrm{S}, +\frac{1}{2}\rangle \rightarrow |6\mathrm{P}, -\frac{1}{2}\rangle$ transition. Transforming (7) into

$$E_\pm = \sqrt{2}E_{(12)}\frac{(\hat{x} \pm \mathrm{i}\hat{y})}{\sqrt{2}}\mathrm{e}^{\mathrm{i}(\vec{k}\cdot\vec{r}-\omega t\mp(\alpha_1+\alpha_2)/2)}C_\pm(x), \tag{8}$$

where

$$C_\pm(x) = \cos\tfrac{1}{2}(\delta\vec{k}\cdot\vec{r} \mp (\alpha_2 - \alpha_1)) = \cos\tfrac{1}{2}(x\delta k \mp (\alpha_2 - \alpha_1)), \tag{9}$$

$\vec{k} = (\vec{k}_1 + \vec{k}_2)/2$ and $\delta\vec{k} = \vec{k}_2 - \vec{k}_1$, we see that the pair of the first two electromagnetic pulses (5) corresponds to the excitation operator

$$\boldsymbol{R}_{(12)} = \sum_{m_I=-\frac{7}{2}}^{+\frac{7}{2}}\sum_{m_J=-\frac{1}{2}}^{+\frac{1}{2}}(a_{m_J}|6\mathrm{S}, m_J, m_I\rangle + b_{m_J}|6\mathrm{P}, -m_J, m_I\rangle)\langle 6\mathrm{S}, m_J, m_I|, \tag{10}$$

where

$$a_{\mp1/2}(\vec{r}) = \cos(\Theta_{(12)}C_\pm(x)/2), \tag{11}$$

$$b_{\mp1/2}(\vec{r}) = \pm\mathrm{i}\mathrm{e}^{\mathrm{i}\vec{k}\cdot\vec{r}}\mathrm{e}^{\mp\mathrm{i}(\alpha_1+\alpha_2)/2}\sin(\Theta_{(12)}C_\pm(x)/2), \tag{12}$$

and m_I is the nuclear spin. Throughout this paper, bold italic is used to indicate an operator. In the above equations, $\Theta_{(12)}$ is the Rabi area of this complex excitation pulse,

$$\Theta_{(12)} = \frac{\sqrt{2}E_{(12)}Dt_p}{\hbar}, \tag{13}$$

where t_p is the duration of the laser pulse and

$$D = \langle 6\mathrm{P}, +\tfrac{1}{2}|\boldsymbol{d}_{+1}|6\mathrm{S}, -\tfrac{1}{2}\rangle = -\langle 6\mathrm{P}, -\tfrac{1}{2}|\boldsymbol{d}_{-1}|6\mathrm{S}, +\tfrac{1}{2}\rangle \tag{14}$$

is the dipole moment matrix element for the transition. The equation (14), with

$$\boldsymbol{d}_{\pm 1} = \vec{\boldsymbol{d}} \cdot \frac{\hat{x} \pm \mathrm{i}\hat{y}}{\sqrt{2}} \tag{15}$$

being the spherical components of the dipole moment operator $\vec{\boldsymbol{d}}$, follows from the Wigner–Eckart theorem.

There are $(2I+1)(2J+1) = 16$ states in the ground and 16 states in the excited energy levels of the investigated transition. Since the caesium atom's thermal energy at room temperature is substantially higher than the hyperfine splitting energy but much smaller than the separation between terminal levels of the transition, the initial state of the caesium atom can be assumed to be on the ground level, with all 16 substates of the ground level equally populated. Therefore, the initial state of caesium atoms in the sample is as follows:

$$|\Psi_0\rangle = \frac{1}{\sqrt{16}} \sum_{m_I=-\frac{7}{2}}^{+\frac{7}{2}} \sum_{m_J=-\frac{1}{2}}^{+\frac{1}{2}} \mathrm{e}^{\mathrm{i}\varphi_{m_J,m_I}} |6\mathrm{S}, m_J, m_I\rangle, \tag{16}$$

where φ_{m_J,m_I} is a random phase factor which is different for each m_J and m_I.

2.2.3. Treatment of the emission problem. According to the rules of billiard-ball dynamics, each crossing between ground and excited state branches of recoil trajectories results in the formation of a macroscopic dipole moment which generates super-radiant emission. The dipole moment that corresponds to crossings at t_c is given by

$$\vec{d}_{t_\mathrm{c}} = \sum_{n,n'} f_{nn'}(t - t_\mathrm{c}) \langle \Psi_n | \vec{\boldsymbol{d}} | \Psi_{n'} \rangle, \tag{17}$$

where the double sum runs over all the trajectories in the crossing branches, $|\Psi_n\rangle$ and $|\Psi_{n'}\rangle$ are the wavefunctions associated with these trajectories and $f_{nn'}(t - t_\mathrm{c})$ is the billiard-ball overlap factor (2). As shown in section 2.1.7, complete overlap can be assumed at $t = t_\mathrm{c}$, so that all $f_{nn'}$'s in (17) are equal:

$$\begin{aligned} f_{nn'}(t - t_\mathrm{c}) \equiv f(t - t_\mathrm{c}) &= \exp\left(-\frac{v_\mathrm{recoil}^2 (t - t_\mathrm{c})^2}{2R_\mathrm{BB}^2}\right) \\ &= \exp\left(-\frac{k^2 (t - t_\mathrm{c})^2 k_\mathrm{B} T}{2m_\mathrm{Cs}}\right) = \exp\left(-\frac{\pi}{4}\frac{(t - t_\mathrm{c})^2}{(T_2^*)^2}\right), \end{aligned} \tag{18}$$

and (17) becomes

$$\vec{d}_{t_\mathrm{c}} = f(t - t_\mathrm{c}) \langle \Psi_{t_\mathrm{c}} | \vec{\boldsymbol{d}} | \Psi_{t_\mathrm{c}} \rangle, \tag{19}$$

where $|\Psi_{t_\mathrm{c}}\rangle = \sum_n |\Psi_n\rangle$.

At each moment t, we represent the state of the system as a sum $|\Psi_{t_\mathrm{c}}\rangle = |6\mathrm{S}\rangle + |6\mathrm{P}\rangle$ where each of the states $|6\mathrm{S}\rangle$ and $|6\mathrm{P}\rangle$ includes those $|\Psi_n\rangle$ that belong, respectively, to the ground and excited state branches of the recoil diagram. In other words, $|6\mathrm{S}\rangle$ or $|6\mathrm{P}\rangle$ represents the state of the whole branch, which, in the further analysis, we treat as a single trajectory. Since $\vec{\boldsymbol{d}}$ only couples $|6\mathrm{S}\rangle$ with $|6\mathrm{P}\rangle$ and is self-adjoint, we can rewrite (19) as

$$\vec{d}_{t_\mathrm{c}} = f(t - t_\mathrm{c}) \langle 6\mathrm{P} | \vec{\boldsymbol{d}} | 6\mathrm{S} \rangle + f(t - t_\mathrm{c}) \langle 6\mathrm{S} | \vec{\boldsymbol{d}} | 6\mathrm{P} \rangle = f(t - t_\mathrm{c}) \langle 6\mathrm{P} | \vec{\boldsymbol{d}} | 6\mathrm{S} \rangle + \mathrm{c.c.} \tag{20}$$

Further, since the macroscopic dipole moment is phased to radiate along the z-axis, we only need the d_x and d_y components of $\vec{d}$. Rather than calculating these two magnitudes directly, we shall find the quantities

$$\tilde{d}_{\pm 1} \equiv \langle 6\mathrm{P} | \boldsymbol{d}_{\pm 1} | 6\mathrm{S} \rangle, \tag{21}$$

whose real parts represent the two orthogonal circularly polarized components of the dipole moment, and then use the relations

$$\begin{cases} d_x = (\tilde{d}_1 + \tilde{d}_{-1})/\sqrt{2} + \text{c.c.} \\ d_y = (\tilde{d}_1 - \tilde{d}_{-1})/\sqrt{2}\mathrm{i} + \text{c.c.} \end{cases} \tag{22}$$

to find $\vec{d}$.

2.2.4. Free decay ($t_c = 0$). The first pair of excitation pulses creates a coherent superposition of the ground and excited states of the caesium atom. Before being inhomogeneously dephased, this coherent superposition gives rise to the FFD. The state of the system develops in time as

$$|\Psi\rangle = \mathrm{e}^{-\mathrm{i}\boldsymbol{H}t/\hbar}\boldsymbol{R}_{(12)}|\Psi_0\rangle, \tag{23}$$

where $\boldsymbol{H}$ is the hyperfine interaction Hamiltonian. We expand (23) as $|\Psi\rangle = |6\mathrm{S}\rangle + |6\mathrm{P}\rangle$ with

$$|6\mathrm{S}\rangle = \tfrac{1}{4} \sum_{m_J, m_I, m'_J, m'_I} a_{m_J} \mathrm{e}^{\mathrm{i}\varphi_{m_J, m_I}} G^{m'_J, m'_I}_{6\mathrm{S}, m_J, m_I}(t)|6\mathrm{S}, m_J, m_I\rangle, \tag{24a}$$

$$|6\mathrm{P}\rangle = \tfrac{1}{4} \sum_{m_J, m_I, m'_J, m'_I} b_{m_J} \mathrm{e}^{\mathrm{i}\varphi_{m_J, m_I}} G^{m'_J, m'_I}_{6\mathrm{P}, -m_J, m_I}(t)|6\mathrm{P}, -m_J, m_I\rangle, \tag{24b}$$

where we have introduced the Green functions

$$G^{m'_J, m'_I}_{L, m_J, m_I}(t) = \langle L, m'_J, m'_I|\mathrm{e}^{-\mathrm{i}\boldsymbol{H}t}|L, m_J, m_I\rangle = \sum_{F=3}^{4} (C^{F, m_J+m_I}_{m_J, m_I})(C^{F, m_J+m_I}_{m'_J, m'_I})\mathrm{e}^{-\mathrm{i}\omega_{L,F}t} \tag{25}$$

in the same manner as in [11]. In the above equation, $\hbar\omega_{L,F}$ is the energy of the hyperfine sublevel F of level L, the latter being either 6S or 6P.

We note two properties of the above functions. First, since the hyperfine interaction conserves the total rotational momentum of the electron and the nucleus, the Green function (25) is nonzero only if

$$m'_I + m'_J = m_I + m_J. \tag{26}$$

Second, there is rotational symmetry that manifests itself as

$$G^{m'_J, m'_I}_{L, m_J, m_I}(t) = G^{-m'_J, -m'_I}_{L, -m_J, -m_I}(t). \tag{27}$$

Since the φ_{m_J, m_I} are randomly distributed, by substituting (24) into (21) we obtain, for $t > 0$:

$$\tilde{d}^{\mathrm{FFD}}_m = \frac{1}{16} \sum_{m_J, m_I, m'_J, m'_I} f(t) a_{m_J} b^*_{m_J} \langle 6\mathrm{P}, m'_J + m, m'_I|\boldsymbol{d}_m|6\mathrm{S}, m'_J, m'_I\rangle \times (G^{m'_J, m'_I}_{6\mathrm{S}, m_J, m_I}(t))(G^{m'_J+m, m'_I}_{6\mathrm{P}, -m_J, m_I}(t))^*. \tag{28}$$

The operator $\boldsymbol{d}_m$ only couples the ground and excited states with equal m_I and opposite m_J, so in (28), $m'_J = -m/2$. Also, applying condition (26) to expression (28), we find that the summation indices in the latter must satisfy

$$\begin{aligned} m'_I + m'_J + m &= m_I - m_J \\ m'_I + m'_J &= m_I + m_J \end{aligned} \tag{29}$$

i.e. $m_I = m'_I$ and $m_J = -m/2$. Therefore, expression (28) for the dipole moment can be rewritten as follows:

$$\tilde{d}_m^{\mathrm{FFD}} = \frac{1}{16}\sum_{m_I} f(t) a_{m_J} b^*_{m_J} \left\langle 6\mathrm{P}, \frac{m}{2}\right| \boldsymbol{d}_m \left| 6\mathrm{S}, -\frac{m}{2}\right\rangle (G^{-\frac{m}{2},m_I}_{6\mathrm{S},-\frac{m}{2},m_I}(t))(G^{\frac{m}{2},m_I}_{6P,\frac{m}{2},m_I}(t))^*. \tag{30}$$

Also using (14) and expanding

$$\begin{aligned}\sin(\tfrac{1}{2}\Theta_{(12)}C_\pm(x))\cos(\tfrac{1}{2}\Theta_{(12)}C_\pm(x)) &= \tfrac{1}{2}\sin(\Theta_{(12)}\cos\{\tfrac{1}{2}[x\delta k \mp (\alpha_2-\alpha_1)]\}) \\ &= \tfrac{1}{2}\sum_{n=-\infty}^{\infty}(-1)^{n+1}J_{2n+1}(\Theta_{(12)})\mathrm{e}^{-\mathrm{i}(2n+1)(x\delta k\mp(\alpha_2-\alpha_1))/2},\end{aligned} \tag{31}$$

where J_m is the mth order Bessel function, we transform equation (30) to the form

$$\tilde{d}_{\pm1}^{\mathrm{FFD}} = -\frac{1}{32}\mathrm{i}Df(t)\mathrm{e}^{-\mathrm{i}(\vec{k}_2\cdot\vec{r}\mp\alpha_2)}A_\pm^{\mathrm{FFD}}(t)\sum_{n=-\infty}^{\infty}(-1)^{n+1}J_{2n+1}(\Theta_{(12)})\mathrm{e}^{-\mathrm{i}n(x\delta k\mp(\alpha_2-\alpha_1))}, \tag{32}$$

where

$$A_\pm^{\mathrm{FFD}}(t) = \sum_{m_I}(G^{\pm1/2,m_I}_{6\mathrm{P},\pm1/2,m_I}(t))^* G^{\mp1/2,m_I}_{6\mathrm{S},\mp1/2,m_I}(t). \tag{33}$$

The macroscopic dipole moment given by (32) is phased to radiate along $\vec{k}_2$, $\vec{k}_2 \pm \delta\vec{k}$, $\vec{k}_2 \pm 2\delta\vec{k}$, etc, which is consistent with the above qualitative analysis (see section 2.1.4).

2.2.5. Stimulated echo fan ($t_\mathrm{c} = \tau$). The third excitation pulse arrives at the moment $t = \tau$. The operator associated with this pulse is

$$\begin{aligned}\boldsymbol{R}_{(3)} = \sum_{m_I=-\frac{7}{2}}^{+\frac{7}{2}}\sum_{m_J=-\frac{1}{2}}^{+\frac{1}{2}} \Bigg\{&\left(\cos\left(\frac{\Theta_{(3)}}{2}\right)|6\mathrm{S}, m_J, m_I\rangle - 2\mathrm{i}\,m_J\mathrm{e}^{\mathrm{i}\vec{k}_3\cdot\vec{r}}\sin\left(\frac{\Theta_{(3)}}{2}\right)|6\mathrm{P}, -m_J, m_I\rangle\right) \\ &\times\langle 6\mathrm{S}, m_J, m_I| + \left(\cos\left(\frac{\Theta_{(3)}}{2}\right)|6\mathrm{P}, m_J, m_I\rangle - 2\mathrm{i}m_J\mathrm{e}^{-\mathrm{i}\vec{k}_3\cdot\vec{r}}\right. \\ &\left.\times\sin\left(\frac{\Theta_{(3)}}{2}\right)|6\mathrm{S}, m_J, m_I\rangle\right)\langle 6\mathrm{P}, -m_J, m_I|\Bigg\},\end{aligned} \tag{34}$$

where

$$\Theta_{(3)} = \frac{\sqrt{2}E_{(3)}Dt_p}{2\hbar} \tag{35}$$

is the pulse's area and $E_{(3)}$ is its electric field amplitude. The state of the system after the third excitation pulse is

$$|\Psi\rangle = \mathrm{e}^{-\mathrm{i}\boldsymbol{H}(t-\tau)/\hbar}\boldsymbol{R}_{(3)}\mathrm{e}^{-\mathrm{i}\boldsymbol{H}\tau/\hbar}\boldsymbol{R}_{(12)}|\Psi_0\rangle, \tag{36}$$

so that

$$\langle\Psi|\vec{\boldsymbol{d}}|\Psi\rangle = \langle\Psi_0|\boldsymbol{R}^\dagger_{(12)}\mathrm{e}^{\mathrm{i}\boldsymbol{H}\tau/\hbar}\boldsymbol{R}^\dagger_{(3)}\mathrm{e}^{\mathrm{i}\boldsymbol{H}(t-\tau)/\hbar}\vec{\boldsymbol{d}}\mathrm{e}^{-\mathrm{i}\boldsymbol{H}(t-\tau)/\hbar}\boldsymbol{R}_{(3)}\mathrm{e}^{-\mathrm{i}\boldsymbol{H}\tau/\hbar}\boldsymbol{R}_{(12)}|\Psi_0\rangle. \tag{37}$$

Extracting those terms in (37) that contribute to the crossing at $t_\mathrm{c} = \tau$, i.e. $|\Psi_{\mathrm{ge}}\rangle$ with $|\Psi_{\mathrm{gg}}\rangle$ and $|\Psi_{\mathrm{ee}}\rangle$ with $|\Psi_{\mathrm{eg}}\rangle$ (figure 3), we obtain, for $t > \tau$:

$$\begin{aligned}\vec{d}^{\,\mathrm{SF}} = f(t-\tau)\{&\langle\Psi_0|(\boldsymbol{R}^{\mathrm{g}\to\mathrm{g}}_{(12)})^\dagger\mathrm{e}^{\mathrm{i}\boldsymbol{H}\tau/\hbar}(\boldsymbol{R}^{\mathrm{g}\to\mathrm{e}}_{(3)})^\dagger\mathrm{e}^{\mathrm{i}\boldsymbol{H}(t-\tau)/\hbar}\vec{\boldsymbol{d}}\mathrm{e}^{-\mathrm{i}\boldsymbol{H}(t-\tau)/\hbar}\boldsymbol{R}^{\mathrm{g}\to\mathrm{g}}_{(3)}\mathrm{e}^{-\mathrm{i}\boldsymbol{H}\tau/\hbar}\boldsymbol{R}^{\mathrm{g}\to\mathrm{g}}_{(12)}|\Psi_0\rangle \\ &+\langle\Psi_0|(\boldsymbol{R}^{\mathrm{g}\to\mathrm{e}}_{(12)})^\dagger\mathrm{e}^{\mathrm{i}\boldsymbol{H}\tau/\hbar}(\boldsymbol{R}^{\mathrm{e}\to\mathrm{e}}_{(3)})^\dagger\mathrm{e}^{\mathrm{i}\boldsymbol{H}(t-\tau)/\hbar}\vec{\boldsymbol{d}}\mathrm{e}^{-\mathrm{i}\boldsymbol{H}(t-\tau)/\hbar}\boldsymbol{R}^{\mathrm{e}\to\mathrm{g}}_{(3)}\mathrm{e}^{-\mathrm{i}\boldsymbol{H}\tau/\hbar}\boldsymbol{R}^{\mathrm{g}\to\mathrm{e}}_{(12)}|\Psi_0\rangle\} \\ &+\mathrm{c.c.}\end{aligned} \tag{38}$$

where the superscripts indicate the components of $\boldsymbol{R}$'s in (10) and (34) associated with the designated transition between the ground ('g') and excited ('e') states. By applying the selection rules for the electric dipole transition along with (26), we transform the above expression into

$$\begin{aligned}\tilde{d}^{\mathrm{SF}}_{\pm 1} = -\frac{1}{16}\sum_{m_I} \mathrm{i}\mathrm{e}^{-\mathrm{i}\vec{k}_3\cdot\vec{r}} f(t-\tau)\sin\Theta_{(3)}\cos\Theta_{(3)} \\ \times\{\cos^2(\tfrac{1}{2}\Theta_{(12)}C_{\pm}(x))G^{\mp\frac{1}{2},m_I}_{6\mathrm{S},\mp\frac{1}{2},m_I}(t)(G^{\mp\frac{1}{2},m_I}_{6\mathrm{S},\mp\frac{1}{2},m_I}(\tau))^*(G^{\pm\frac{1}{2},m_I}_{6\mathrm{P},\pm\frac{1}{2},m_I}(t-\tau))^* \\ +\cos^2(\tfrac{1}{2}\Theta_{(12)}C_{\mp}(x))G^{\mp\frac{1}{2},m_I\pm 1}_{6\mathrm{S},\pm\frac{1}{2},m_I}(t)(G^{\mp\frac{1}{2},m_I\pm 1}_{6\mathrm{S},\pm\frac{1}{2},m_I}(\tau))^*(G^{\pm\frac{1}{2},m_I\pm 1}_{6\mathrm{P},\pm\frac{1}{2},m_I\pm 1}(t-\tau))^* \\ -\sin^2(\tfrac{1}{2}\Theta_{(12)}C_{\pm}(x))(G^{\pm\frac{1}{2},m_I}_{6\mathrm{P},\pm\frac{1}{2},m_I}(t))^*G^{\pm\frac{1}{2},m_I}_{6\mathrm{P},\pm\frac{1}{2},m_I}(\tau)G^{\mp\frac{1}{2},m_I}_{6\mathrm{S},\mp\frac{1}{2},m_I}(t-\tau) \\ -\sin^2(\tfrac{1}{2}\Theta_{(12)}C_{\mp}(x))(G^{\pm\frac{1}{2},m_I\mp 1}_{6\mathrm{P},\mp\frac{1}{2},m_I}(t))^*G^{\pm\frac{1}{2},m_I\mp 1}_{6\mathrm{P},\mp\frac{1}{2},m_I}(\tau)G^{\mp\frac{1}{2},m_I\mp 1}_{6\mathrm{S},\mp\frac{1}{2},m_I\mp 1}(t-\tau)\}. \quad (39)\end{aligned}$$

Converting the grating factors

$$\sin^2(\tfrac{1}{2}\Theta_{(12)}C_{\pm}(x)) = \tfrac{1}{2} - \tfrac{1}{2}\cos(\Theta_{(12)}C_{\pm}(x)) \quad (40a)$$

$$\cos^2(\tfrac{1}{2}\Theta_{(12)}C_{\pm}(x)) = \tfrac{1}{2} + \tfrac{1}{2}\cos(\Theta_{(12)}C_{\pm}(x)), \quad (40b)$$

we note that in the right-hand side of (40*a*, *b*), it is only the second term that constitutes transient induced grating and needs to be given further consideration. Expanding it into the Fourier series

$$\cos(\Theta_{(12)}C_{\pm}(x)) = \sum_{m=-\infty}^{\infty} J_{2n}(\Theta_{(12)})(-1)^n\mathrm{e}^{\mathrm{i}n(-x\delta k\pm(\alpha_2-\alpha_1))} \quad (41)$$

transforms (39) into

$$\begin{aligned}\tilde{d}^{\mathrm{SF}}_{\pm 1} = -\frac{1}{32}\mathrm{i}D\mathrm{e}^{-\mathrm{i}\vec{k}_3\cdot\vec{r}} f(t-\tau)\sin\Theta_{(3)}\cos\Theta_{(3)} \\ \times\sum_{n=-\infty}^{\infty} J_{2n}(\Theta_{(12)})(-1)^n\mathrm{e}^{-nx\delta k}(A^{\mathrm{SF}}_{\pm}(t,\tau)\mathrm{e}^{\pm n(\alpha_2-\alpha_1)} + B^{\mathrm{SF}}_{\pm}(t,\tau)\mathrm{e}^{\mp n(\alpha_2-\alpha_1)}),\end{aligned} \quad (42)$$

where

$$\begin{aligned}A^{\mathrm{SF}}_{\pm}(t,\tau) = \sum_{m_I} G^{\mp\frac{1}{2},m_I}_{6\mathrm{S},\mp\frac{1}{2},m_I}(t)(G^{\mp\frac{1}{2},m_I}_{6\mathrm{S},\mp\frac{1}{2},m_I}(\tau))^*(G^{\pm\frac{1}{2},m_I}_{6\mathrm{P},\pm\frac{1}{2},m_I}(t-\tau))^* \\ +\sum_{m_I}(G^{\pm\frac{1}{2},m_I}_{6\mathrm{P},\pm\frac{1}{2},m_I}(t))^*G^{\pm\frac{1}{2},m_I}_{6\mathrm{P},\pm\frac{1}{2},m_I}(\tau)G^{\mp\frac{1}{2},m_I}_{6\mathrm{S},\mp\frac{1}{2},m_I}(t-\tau)\end{aligned} \quad (43)$$

is associated with the evolution process where the quantum number m_J is conserved, and

$$\begin{aligned}B^{\mathrm{SF}}_{\pm}(t,\tau) = \sum_{m_I} G^{\mp\frac{1}{2},m_I\pm 1}_{6\mathrm{S},\pm\frac{1}{2},m_I}(t)(G^{\mp\frac{1}{2},m_I\pm 1}_{6\mathrm{S},\pm\frac{1}{2},m_I}(\tau))^*(G^{\pm\frac{1}{2},m_I\pm 1}_{6\mathrm{P},\pm\frac{1}{2},m_I\pm 1}(t-\tau))^* \\ +\sum_{m_I}(G^{\pm\frac{1}{2},m_I\mp 1}_{6\mathrm{P},\mp\frac{1}{2},m_I}(t))^*G^{\pm\frac{1}{2},m_I\mp 1}_{6\mathrm{P},\mp\frac{1}{2},m_I}(\tau)G^{\mp\frac{1}{2},m_I\mp 1}_{6\mathrm{S},\mp\frac{1}{2},m_I\mp 1}(t-\tau)\end{aligned} \quad (44)$$

where it is not. In agreement with the previous analysis, the dipole moment (42) is phased along $\vec{k}_3 + n\,\delta\vec{k}$.

2.2.6. Two-pulse echo fan ($t_c = 2\tau$). As time t approaches the value of 2τ, the billiard balls associated with the states $|\Psi_{eg}\rangle$ and $|\Psi_{ge}\rangle$ start to overlap, resulting in a macroscopic dipole moment manifesting itself as a two-pulse photon echo fan (EF). Extracting appropriate terms in (37) we find, for $t > \tau$:

$$\vec{d}^{\,\mathrm{EF}} = f(t-2\tau)\langle\Psi_0|(\boldsymbol{R}_{(12)}^{\mathrm{g}\to\mathrm{g}})^\dagger \mathrm{e}^{\mathrm{i}\boldsymbol{H}\tau/\hbar}(\boldsymbol{R}_{(3)}^{\mathrm{g}\to\mathrm{e}})^\dagger \times \mathrm{e}^{\mathrm{i}\boldsymbol{H}(t-\tau)/\hbar}\vec{\boldsymbol{d}}\mathrm{e}^{-\mathrm{i}\boldsymbol{H}(t-\tau)/\hbar}\boldsymbol{R}_{(3)}^{\mathrm{e}\to g}\mathrm{e}^{-\mathrm{i}\boldsymbol{H}\tau/\hbar}\boldsymbol{R}_{(12)}^{\mathrm{g}\to\mathrm{e}}|\Psi_0\rangle + \mathrm{c.c.} \tag{45}$$

This expression, on application of the selection rules and expanding the transient induced grating factor into Fourier series (31), transforms into

$$\tilde{d}_{\pm1}^{\mathrm{EF}} = \frac{1}{32}\mathrm{i}Df(t-2\tau)\mathrm{e}^{-\mathrm{i}(2\vec{k}_3-\vec{k}_1)\cdot\vec{r}}\sin^2\Theta_{(3)}\sum_{n=-\infty}^{\infty}(-1)^{n+1}J_{2n+1}(\Theta_{(12)})\mathrm{e}^{-\mathrm{i}nx\delta k} \times(\mathrm{e}^{\mp\mathrm{i}\alpha_1\pm\mathrm{i}n(\alpha_2-\alpha_1)}A_{\pm}^{\mathrm{EF}}(t,\tau) + \mathrm{e}^{\pm\mathrm{i}\alpha_1\mp\mathrm{i}n(\alpha_2-\alpha_1)}B_{\pm}^{\mathrm{EF}}(t,\tau)). \tag{46}$$

where the evolution factors

$$A_{\pm}^{\mathrm{EF}}(t,\tau) = \sum_{m_I}(G_{6\mathrm{P},\pm\frac{1}{2},m_I}^{\pm\frac{1}{2},m_I}(t-\tau))^*(G_{6\mathrm{S},\mp\frac{1}{2},m_I}^{\mp\frac{1}{2},m_I}(\tau))^*G_{6\mathrm{S},\mp\frac{1}{2},m_I}^{\mp\frac{1}{2},m_I}(t-\tau)G_{6\mathrm{P},\pm\frac{1}{2},m_I}^{\pm\frac{1}{2},m_I}(\tau) \tag{47}$$

and

$$B_{\pm}^{\mathrm{EF}}(t,\tau) = \sum_{m_I}(G_{6\mathrm{P},\pm\frac{1}{2},m_I\pm1}^{\pm\frac{1}{2},m_I\pm1}(t-\tau))^*(G_{6\mathrm{S},\pm\frac{1}{2},m_I}^{\mp\frac{1}{2},m_I\pm1}(\tau))^*G_{6\mathrm{S},\pm\frac{1}{2},m_I}^{\mp\frac{1}{2},m_I\pm1}(t-\tau)G_{6\mathrm{P},\pm\frac{1}{2},m_I}^{\pm\frac{1}{2},m_I}(\tau) + \sum_{m_I}(G_{6\mathrm{P},\mp\frac{1}{2},m_I}^{\pm\frac{1}{2},m_I\mp1}(t-\tau))^*(G_{6\mathrm{S},\mp\frac{1}{2},m_I}^{\mp\frac{1}{2},m_I}(\tau))^*G_{6\mathrm{S},\mp\frac{1}{2},m_I\mp1}^{\mp\frac{1}{2},m_I\mp1}(t-\tau)G_{6\mathrm{P},\mp\frac{1}{2},m_I}^{\pm\frac{1}{2},m_I\mp1}(\tau) \tag{48}$$

are defined analogous to those in equation (42).

Note that for all three types of CFE it follows from equation (27) that

$$\begin{aligned} A_+(t) &= A_-(t) \\ B_+(t) &= B_-(t) \end{aligned}. \tag{49}$$

2.2.7. Polarization properties. It is instructive to analyse equations (32), (42) and (46) for the case when there is no hyperfine splitting in the ground or excited level. If so, for all three fans, $A_\pm(t) = 1$ and $B_\pm(t) = 0$. As a result, the amplitudes of $\tilde{d}_{+1}$ and $\tilde{d}_{-1}$ are the same, and the superposition of the two circularly polarized fields they create yields a linearly polarized field (22). The polarization angle of this field is given by

$$\alpha_n^{\mathrm{FFD}} = \alpha_2 + n(\alpha_2 - \alpha_1) \tag{50}$$

for the nth component of the FFD,

$$\alpha_n^{\mathrm{SF}} = n(\alpha_2 - \alpha_1) \tag{51}$$

for the stimulated fan (SF) and

$$\alpha_n^{\mathrm{EF}} = -\alpha_1 + n(\alpha_2 - \alpha_1) \tag{52}$$

for the two-pulse EF, as shown in figure 4. The results (50)–(52) can be intuitively understood as follows. First, (50) is straightforward for the FFD components with n equal to 0 and -1: these two components are just the free polarization decay fields brought about by the two excitation pulses and should have the same polarization as the latter. For $n = -2$ and $n = 1$, the relation (50) obtains if these two components of the FFD are considered as

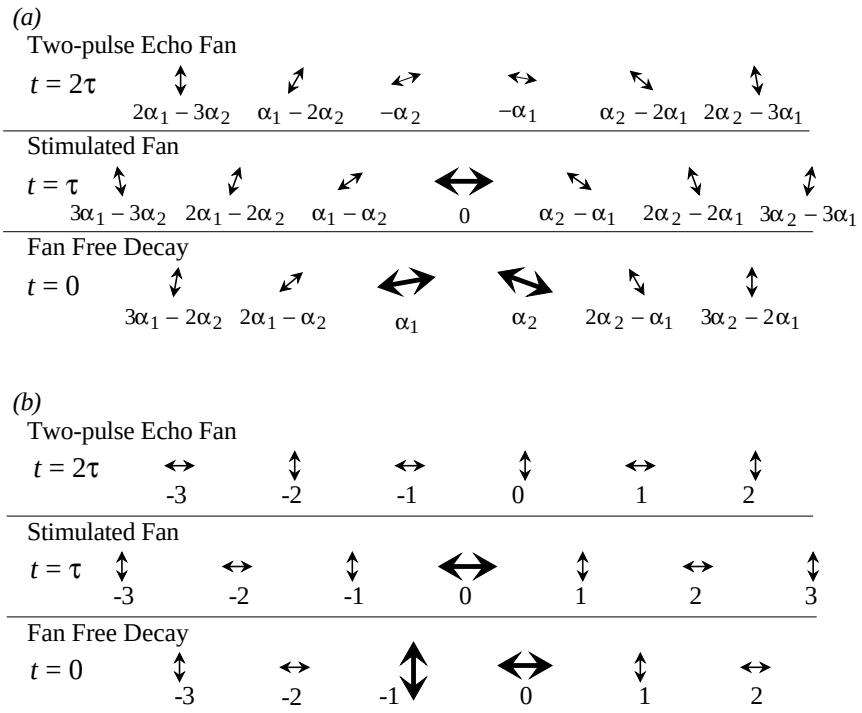

Figure 4. CFE polarization angles in several first orders. The excitation pulses are shown with heavy lines. (*a*) The polarization angles in the case of a two-level system for arbitrarily polarized excitation pulses. In (*b*) we specialize to our experimental conditions of $\alpha_1 = 90^\circ$, $\alpha_2 = 0^\circ$. Each CFE component is numbered according to (32), (42) and (46).

two-pulse photon echoes caused by the first two excitation pulses. It is known [13] that a two-pulse echo is linearly polarized at the angle

$$\alpha_{\text{echo}} = 2\alpha_2 - \alpha_1 \tag{53}$$

if the first and second excitation pulses are polarized at angles α_1 and α_2, respectively. The result (50) for other values of n can be obtained by regarding the nth FPD component as a two-pulse photon echo with respect to the $(n-1)$th and $(n-2)$th components and applying the equation (53) successively to all values of n. Similarly, the relations (51), (52) can be derived by considering the SF or EF component as, respectively, a stimulated or two-pulse photon echo caused by one of the FFD components and the third excitation pulse.

Equation (53), originally derived for a simplistic two-level system, holds true for the photon echoes in caesium vapour only if hyperfine interaction is neglected. So do results (50)–(52). The quantities $A(t,\tau)$ and $B(t,\tau)$ in the equations (42) and (46) are complex numbers, and yield, generally speaking, unequal results for the amplitudes of $\tilde{d}_{+1}$ and $\tilde{d}_{-1}$ when multiplied by phase factors and added. Therefore, the FPE in the considered system are normally elliptically polarized.

However, if the first two excitation pulses are polarized along or normal to the polarization of the third pulse, the relative phase factors in front of $A_\pm(t)$ and $B_\pm(t)$ in the equations (42) and (46) are real. Thus, and because of the relations (49), all the CFE components are linearly polarized as shown in figure 4(*b*) (specialized to $\alpha_1 = \pi/2$, $\alpha_2 = 0$) and the relations (50)–(52) stay valid. For given τ, the intensity temporal profile of the

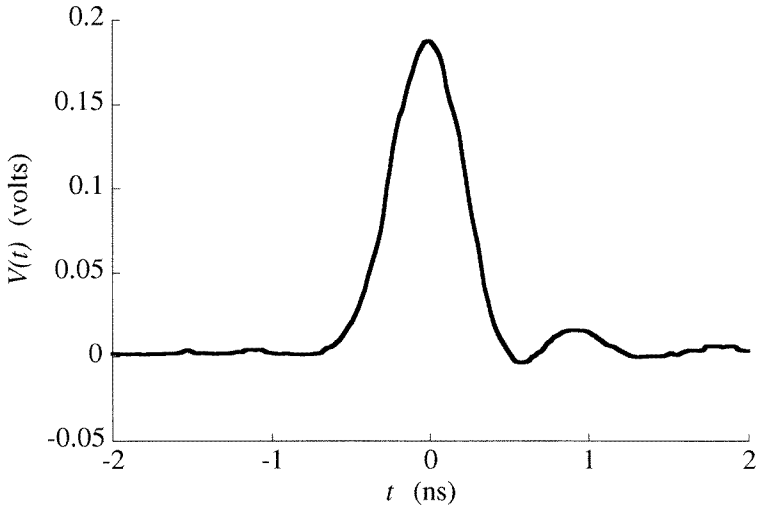

Figure 5. The detector response function as displayed on a Tektronix 7104 mainframe using a 7A29 input amplifier. It responds to the output of a 1 GHz bandwidth 'fast FND' which is irradiated by a 10 ps optical excitation pulse. The zero of time is chosen at the peak of the response so that the displayed intensity will appear undelayed by the 'slow' detector response. This facilitates comparison between experimental measurements and theory.

stimulated and two-pulse fan components should then only depend on whether n is even or odd. This case was realized in our experiment.

2.2.8. Modulation properties. The intensity of the nth CFE component is proportional to

$$I^{(n)}(t,\tau) \propto (\tilde{d}_{+1}^{(n)})^2 + (\tilde{d}_{-1}^{(n)})^2 \tag{54}$$

where $\tilde{d}_{\pm 1}^{(n)}$ stands for the nth term of the sum in expressions (32), (42) and (46). The intensity (54) is modulated with the frequencies of the hyperfine splitting in the ground and the excited states. To be compared with experimentally observed oscilloscope traces, this intensity had to be convolved with the photodetector response function $V(t)$ (figure 5). The latter was obtained as the photodetector's response to a short (10 ps) laser pulse.

The expression (54) assumes the validity of the phase matching condition [14]

$$(\phi_{(i)}^{(n)})^2 \ll \frac{\lambda}{L}, \tag{55}$$

where $\phi_{(i)}^{(n)}$ is the angle between the nth fan component and the ith excitation pulse and $L = 1$ cm is the thickness of the sample. If this inequality does not hold, the intensity of a component will diminish.

3. Experiment

The sample was excited with spectrally filtered [15], amplified 894 nm pulses from a Spectra Physics 375B dye laser synchronously pumped by a Spectra Physics series 3000 Nd-YAG laser. These pulses were characterized by energies up to 1 μJ, a close to transform limited spectrum and a 10 ps width. All hyperfine sublevels were equally excited. The schematic diagram of the optical set-up is shown in figure 6. Emerging from the amplifier, circularly

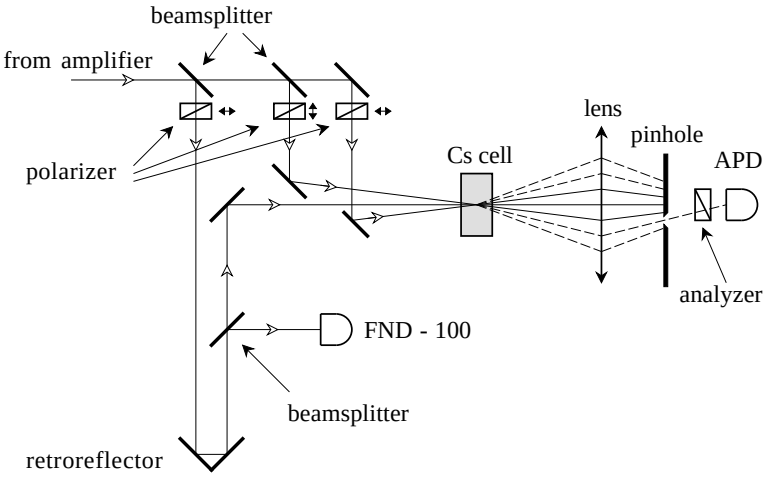

Figure 6. A schematic diagram of the CFE experiment.

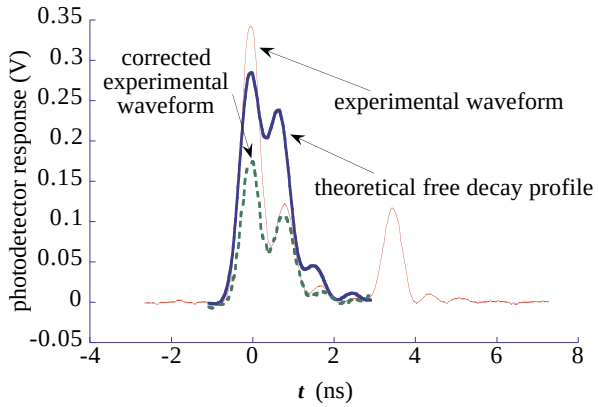

Figure 7. The experimental waveform of the FFD component at $n = 2$ is shown with a full curve along with the theoretically expected one. The heavy dotted curve is the result of subtracting a background waveform (taken with the detuned laser) from the signal waveform (taken with the laser at resonance).

polarized pulses were split into three with a system of beamsplitters and mirrors so that the first two pulses were sent into the cell simultaneously, and the third one at a variable delay. All three pulses went through Glan prisms which rendered one of the first two pulses vertically and the other two horizontally polarized. The three excitation pulses entered the sample along three noncoplanar directions. Thus k vectors formed a pyramid with an equilateral triangle base and each angle at the apex about 0.003 rad. The two lenses and a pinhole behind the sample formed a spatial filter facilitating selection of the required fan component by moving the pinhole in the vertical plane, according to figure 4. The CFE signals were registered by a 1 GHz bandwidth EG&G C30902E avalanche photodiode (APD), connected to a 1 GHz Tektronix A7129 amplifier mounted in a 7104 oscilloscope mainframe. The intensity of the excitation pulses was also monitored with a EG&G FND-100 silicon photodiode (FND). The synchronism between the first two pulses was determined

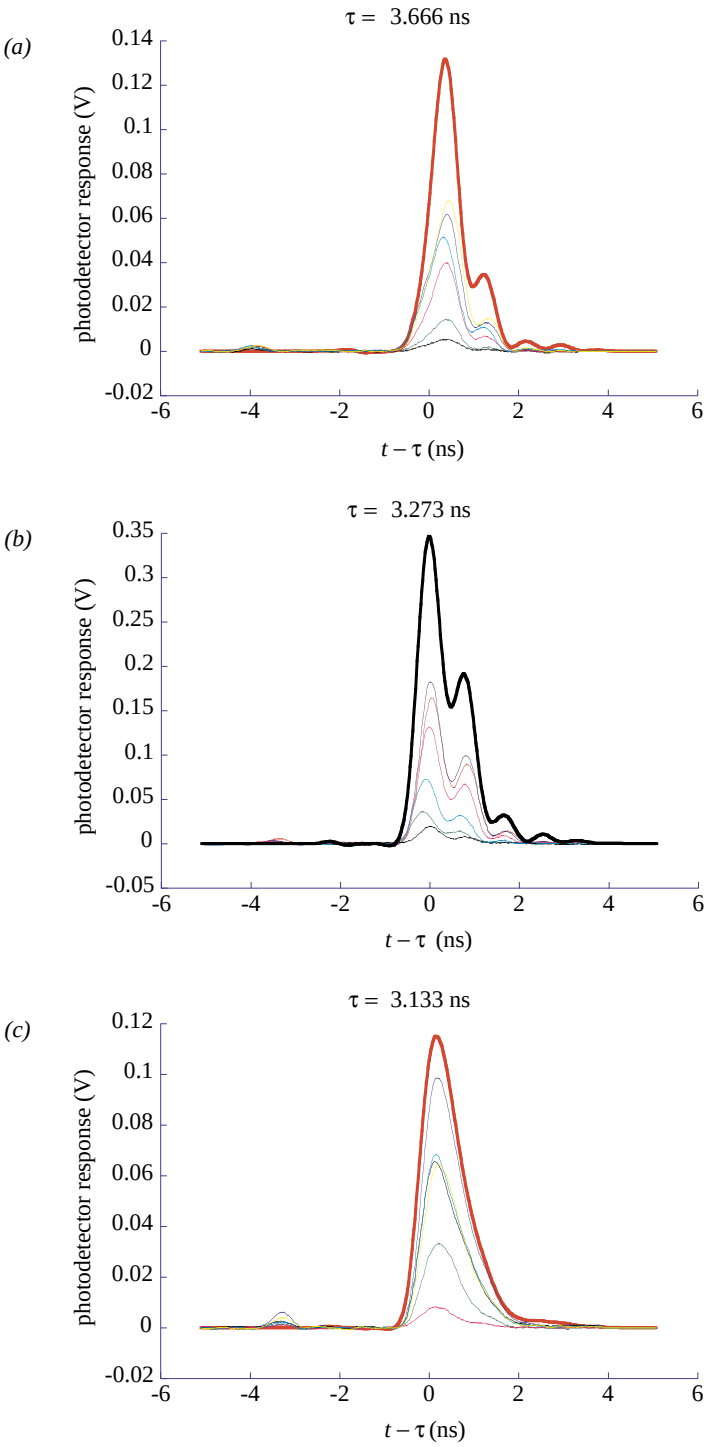

Figure 8. The $n = 1$ SF component oscilloscope traces are shown along with their theoretical prediction (heavy curve) for three different values of the delay τ.

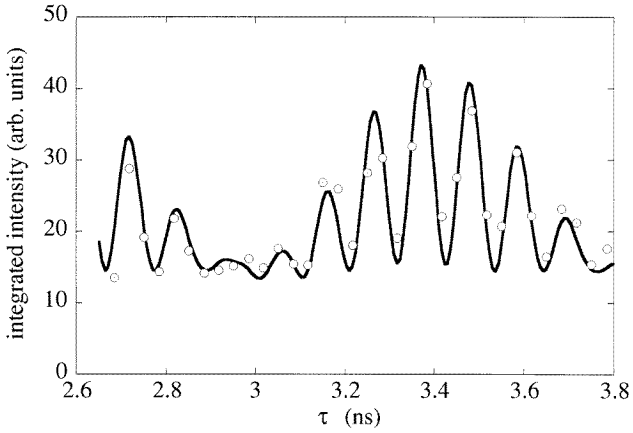

Figure 9. Experimental data of the integrated SF $n = 1$ component as a function of τ. The full trace is the theoretical fit done by varying the scale and background values.

by observing the EF, the delay τ of the third pulse was found with an error of about 40 ps via the technique described in [11].

Our sample was a 1 cm long quartz cell containing saturated caesium vapour at about 45 °C. Measurements performed in [11] showed that at this temperature the sample remains optically thin so that propagation effects had no effect on CFE intensity patterns.

All the CFE components shown in figure 4 were actually observed in the experiment. The polarization of each component was determined by rotating an analyser in front of the APD detector and was found to be consistent with what was theoretically predicted. The signals observed when the analyser was rotated by 90° from the expected polarization were degraded by at least 95%.

The observed CFE signals in the experiment exhibited dramatic quantum beats associated with the 1 GHz hyperfine splitting of the 6P level. The beats caused by the 9 GHz hyperfine structure of the ground level have not been observed because they were beyond the bandwidth of our electronics. The unique quantum beat structure of each of the CFE components provided us with a kind of signature that facilitated comparison of theoretical results with experiments.

A typical oscilloscope trace corresponding to the first FFD component is shown in figure 7. Since the polarization of one of the first two excitation pulses was the same as that of the observed FFD component, we were unable to fully eliminate the leakage of this pulse through the spatial filter. The oscilloscope trace thus displayed a combination of the contributions from the FD signal and the leaking excitation pulse. In order to determine what part of the observed trace was due to this leakage we performed a set of measurements with the dye laser detuned from resonance so that there was no FD signal entering the detector. In this case the traces exhibited substantially lower intensity and different shape. The dotted curve in figure 7 shows the result of subtracting the oscilloscope waveforms obtained with the laser in and out of resonance. This gave us the shape of the free decay signal and is in good agreement with the theoretically expected one plotted in figure 7 with a heavy full curve.

Figures 8(*a*)–(*c*) present the shapes of the first ($n = 1$) SF component at three different values of the delay τ. Since this signal was vertically polarized, whereas the third excitation pulse was polarized horizontally, it was possible to completely eliminate the leakage of the

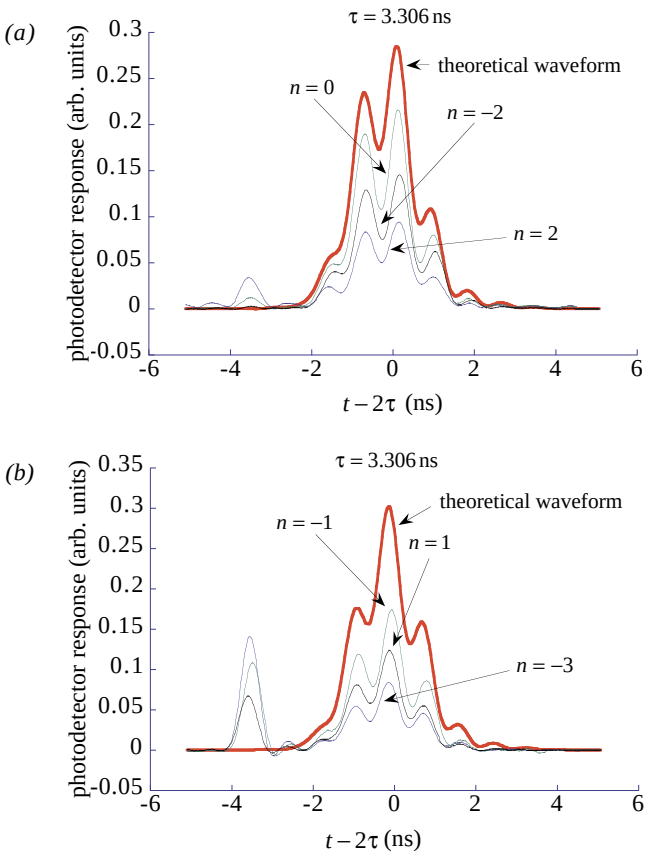

Figure 10. Typical experimental two-pulse echo traces for even (*a*) and (*c*) and odd (*b*) and (*d*) values of n are shown for two values of τ. The scale of each waveform is arbitrary, the heavy curve shows the theoretically predicted waveform.

latter, so that the above correction was not necessary. Each graph shows six waveforms acquired with six laser shots. Good reproducibility and excellent agreement with theory are achieved.

We also performed a set of measurements of the time integrated intensity of the first SF component versus delay τ. The output of the avalanche photodetector was directed into a Stanford Research Systems gated integrator. For each value of a delay, integration of 100 echo pulses over the 40 ns gate was performed. The average values of the integral are plotted in figure 9 along with the theoretical fit obtained by varying its vertical scale and background value. Unlike the time-dependent intensity patterns, both ground and excited state hyperfine modulations are resolved here.

Finally, we have obtained oscilloscope traces of the two-pulse EF up to its third component. As expected (figure 10), the shapes of the echo waveforms for given τ only depend on whether n is odd or equal.

There is an obvious difference between the intensity patterns of the EF emissions and other types of CFEs. The former are practically symmetric with respect to the point $t = 2\tau$ (figure 10), while the latter quickly fall off for $t < 0$ (FFD, figure 7) and $t < \tau$ (SF, figure 8). This behaviour is readily understood as the echoes arise from a rephasing process

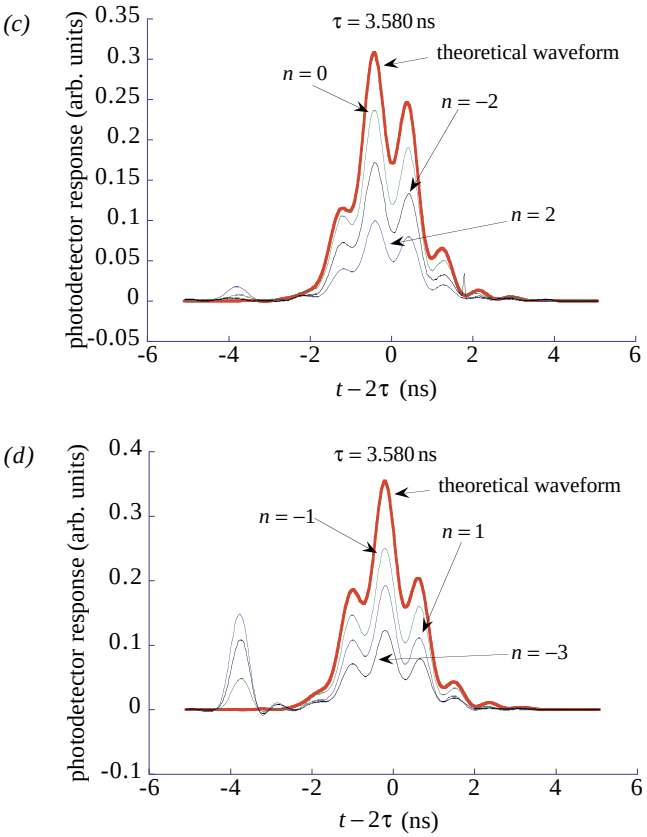

Figure 10. (Continued)

while the FFD's and SF's are generated at the exact moment the associated excitation pulses are applied. Thus echoes last for a time of order $2T_2^*$ while the FFDs and SFs last for only half that time.

Most of the CFE oscilloscope waveforms are modulated with the 1.168 GHz frequency of the 6P state hyperfine splitting. The depth of modulation depends on n and τ; for example, the odd n SF components with $\tau = 3.133$ ns (figure 8(c)) experience very minor modulation. The exact shape and symmetry of each intensity pattern depends on the relative position of the bell-shaped BBM overlap factor with respect to modulation peaks [11]. For odd values of n and $\tau = 3.580$ ns the signals are symmetric since the overlap factor $f^2(t - 2\tau)$ is centred over one of the peaks (see figure 10(d)). For even n they are asymmetric as $f^2(t - 2\tau)$ is centred between two of them (figure 10(c)).

Note that some of the experimental oscilloscope traces of CFE components exhibit peaks that are located on the right- (figure 7) and left-hand sides (figures 8 and 10) of the main waveform and not accounted for by the theory. These peaks are associated with either the first two or the third excitation pulses leaking through the spatial filter.

4. Conclusion

We have demonstrated that by exciting the sample with two simultaneous strong short laser pulses one obtains the prompt emission of a multitude of coherent FFD signals. These signals are characterized by the same modulation properties as normal single-pulse free decay signal but are easier to observe because of their spatial separation from the two laser beams.

If the two simultaneous excitation pulses at $t = 0$ are followed by the delayed third pulse at $t = \tau$, one observes two additional types of CFE, stimulated echo fan emitted immediately following the third pulse and two-pulse EF centred at $t = 2\tau$. Each component of these fans has a unique modulation and polarization pattern which is determined by the atomic Hamiltonian. This feature demonstrates the potential of this technique as a spectroscopic tool.

References

[1] Phillion D W, Kuizenga D J and Siegman A E 1975 *Appl. Phys. Lett.* **27** 85
[2] Yajima T and Taira Y 1979 *J. Phys. Soc. Japan* **48** 1620
[3] Weiner A M, Silvestri S D and Ippen E P 1985 *J. Opt. Soc. Am.* B **2** 654
[4] Mossberg T W *et al* 1979 *Phys. Rev. Lett.* **43** 851
[5] Friedberg R and Hartmann S R 1993 *Laser Phys.* **3** 526
[6] Beach R, Hartmann S R and Friedberg R 1982 *Phys. Rev.* A **25** 2658
[7] Friedberg R and Hartmann S R 1993 *Phys. Rev.* A **48** 1446
[8] Friedberg R and Hartmann S R 1994 *Bull. Russ. Acad. Sci.* **58** 1282
[9] Brewer R G and Shoemaker R L 1972 *Phys. Rev.* A **6** 2001
[10] Brownell J H, Lu X and Hartmann S R 1995 *Phys. Rev. Lett.* **75** 3657
[11] Lvovsky A I and Hartmann S R 1996 *Laser Phys.* **6** 535
[12] Weber K-H and Sansonetti C J 1987 *Phys. Rev.* A **35** 4650
[13] Abella I D, Kurnit N A and Hartmann S R 1966 *Phys. Rev.* **141** 391
[14] Kurnit N A, Abella I D and Hartmann S R 1964 *Phys. Rev. Lett.* **13** 567
[15] Lu X, Brownell J H and Hartmann S R 1995 *Opt. Commun.* **120** 295